Margin Balancing Control Design of Three-Phase Grid-Tied PV Inverters for Stability Improvement

Zhiqing Yang, *Student Member, IEEE*, Tianxiao Chen, *Student Member, IEEE*, Xian Luo, Philipp Schülting, and Rik W. De Doncker, *Fellow, IEEE*

***Abstract*—Frequency responses are nonidentical between the positive and the negative frequency range for symmetric three-phase systems modeled with complex transfer functions, which shows unbalanced stability margins. The unbalanced stability margins limit the system performance, as the system dynamics are restricted by the worst one. This article extends the discussion of unbalanced stability margins to asymmetric three-phase systems, i.e., three-phase grid-tied inverters, which are described by transfer matrices. The reason for unbalanced stability margins is analytically investigated, and different impacts are analyzed. It is found that both the control delay and asymmetric control loops can lead to the unbalanced stability margins. To improve the performance limited by the worst stability margin, a margin balancing control is proposed. By implementing a phase correction term, the worst stability margin can be increased by reducing the best one. As a result, the overall stability margin of the system can be improved. The design procedure is elaborated based on a 2-MW inverter system. Verifications are presented based on a 1-kW prototype including simulations, experimental results, and Nyquist analyses. This method applies to all types of grid-tied inverters with multiple control loops.**

***Index Terms*—Asymmetric system, grid-tied converter, impedance model (IM), stability margin, transfer matrices.**

I. Introduction

THREE-PHASE systems are popular in power conversion and electrical drive applications. Different from a single-phase system, which can be usually modeled with a single-input single-output (SISO) structure, a three-phase system is described by a multi-input multi-output (MIMO) structure due to the multiphase feature. In order to analyze the dynamics of three-phase systems, Park or Clarke transformation is used to convert variables from a three-dimensional abc frame to a 2-D dq or $\alpha\beta$ frame [1]. However, the system still remains a MIMO structure. Thus, proper mathematical tools are expected to facilitate the modeling and the control design of three-phase systems.

Symmetric three-phase systems can be further simplified to complex SISO systems utilizing complex vectors and complex transfer functions [2]. The in-phase quantity is expressed with the real part, while the cross-coupling quantity is represented with the imaginary part. Complex transfer functions benefit the control design of systems with highly coupled channels, e.g., systems modeled in the dq frame. They are used to design the alternating-current control (ACC) for motor drive applications [3]–[5], and the alternating-voltage control for ac power supply systems [6]. It should be pointed out that, compared to convention SISO systems, the analysis range of complex SISO systems is extended from $0 < \omega < \infty$ to $-\infty < \omega < \infty$.

For grid-tied applications, asymmetric control loops, i.e., the phase-locked loop (PLL) and the direct-voltage control (DVC) are usually implemented. The PLL synchronizes the injected current by regulating the q-axis grid voltage, which introduces the asymmetry in the q-axis [7]. The DVC regulates the dc-link voltage by commanding the d-axis reference current, which introduces the asymmetry in the d-axis [8]. To describe the dynamics of asymmetric three-phase systems represented by complex vectors, two complex transfer functions are required [9]. Consequently, the system cannot be treated as a SISO system anymore, and mathematical efforts are required to deal with two complex transfer functions simultaneously [10]. A more general approach to deal with MIMO systems is the transfer matrix. By converting complex vectors to real vectors, the dynamics of asymmetric systems can be described by transfer matrices [9]. The in-phase quantity is expressed with diagonal elements, while the cross-coupling quantity is represented with off-diagonal elements. Transfer matrices are used to design the ACC for ac machines that are featured with asymmetric properties due to the pole saliency [11], [12], and to investigate the harmonic stability of grid-tied inverters that are featured with asymmetric control structures [7], [8].

Since symmetric three-phase systems can be simplified as complex SISO systems, the control design of which can follow the classic control theory for conventional SISO systems utilizing the concept of stability margins [13]. However, due to the extended frequency range for analyses, there are two stability

Manuscript received November 7, 2020; revised January 26, 2021; accepted February 17, 2021. Date of publication February 23, 2021; date of current version June 1, 2021. This work was supported by the German Federal Ministry for Economic Affairs, and Energy under Grant BMWi, FKZ0324211D, PV-Kraftwerk2025. Recommended for publication by Associate Editor F. Wang. *(Corresponding author: Zhiqing Yang.)*

Zhiqing Yang, Tianxiao Chen, and Rik W. De Doncker are with the Institute for Power Generation and Storage Systems, E.ON Energy Research Center, RWTH Aachen University, 52074 Aachen, Germany (e-mail: zhiqing.yang@eonerc.rwth-aachen.de; tianxiao.chen@foxmail.com; post_pgs@eonerc.rwth-aachen.de).

Xian Luo was with the Institute for Power Generation and Storage Systems, E.ON Energy Research Center, RWTH Aachen University, 52074 Aachen, Germany. She is now with Huawei Technologies Co., Ltd, Shanghai 201206, China (e-mail: xian.luo@rwth-aachen.de).

Philipp Schülting was with the Institute for Power Electronics and Electrical Drives, RWTH Aachen University, 52066 Aachen, Germany. He is now with EA Elektro-Automatik GmbH, 41747, Viersen, Germany (e-mail: philipp.schuelting@isea.rwth-aachen.de).

Digital Object Identifier 10.1109/TPEL.2021.3061624

margins in complex SISO systems, which are located in the positive and the negative frequency range individually. Unbalanced stability margins are observed in complex SISO systems, and the controller stability is limited by the worst one [14]–[16]. It is found that the reasons for unbalanced stability margins are the control delay and the cross-coupling effect [14]. Although the latter influence can be usually compensated by implementing decoupling terms utilizing state feedbacks, stability margins are still unbalanced, which leads to unsatisfied transient performances. To further improve the transient performance of complex SISO systems, a complex phase correction (PC) is considered in [14] and [15], so that the worst stability margin can be increased by reducing the best one, which leads to better dynamic performances. However, the suggested implementation only compensates the impact of the control delay without providing any clear design rules. The idea is further implemented in grid-tied inverter systems with LCL filters [15]. An optimal PC angle is suggested as the average value of the best and the worst stability margin. However, the developed model considers only the ACC, while neglects the PLL and DVC, which cannot describe the complete dynamics in grid-tied inverter systems.

Mathematical efforts are made to simplify MIMO systems to SISO ones, when analyzing the harmonic stability of grid-tied converters [17]–[20], which is strongly influenced by the PLL and the grid stiffness. The three-phase grid-tied inverter can be simplified to multiple SISO models in either the sequence domain [17] or the dq domain [18]. However, the system performance is determined by the total influence of all SISO models. Although the harmonic stability can be investigated by applying the Nyquist criterion on individual SISO models, the control design cannot simply follow the rules that apply to conventional SISO systems, as a modification of control structures can influence all SISO models simultaneously. SISO models can reveal the negative-resistance effect induced by the PLL [19], [20]. Based on that, control methods are developed to compensate the adverse influence of the PLL through the impedance shaping [19], [20]. However, unbalanced stability margins may still exist, which can be further optimized.

If transfer matrices are used to model asymmetric three-phase systems, a MIMO system can be described by a 2-D matrix instead of multiple complex transfer functions. As complete dynamics are included in a single matrix, the system stability can be improved by designing the control for the single matrix. However, several aspects require further investigations, as follows. 1) As stability margins for MIMO systems are not clearly defined [21], it is difficult to develop control methods to improve their stability margins quantitatively. 2) Nyquist curves are mirror-symmetric between the positive and the negative frequency range for systems described by transfer matrices [7]. How to observe and compensate unbalanced stability margins needs to be explored.

To improve the harmonic stability of three-phase grid-tied inverters influenced by asymmetric control loops, this article proposes a new framework to investigate stability margins of MIMO systems quantitatively. Based on that, a control method is proposed to improve the system stability margin. Main contributions are summarized as follows.

a) Based on the proposed phase margin (PM) definitions for MIMO systems containing multiple eigenvalues, unbalanced stability margins are investigated for asymmetric three-phase systems described by transfer matrices. The impact of different factors on the unbalanced stability margins is quantitatively studied.
b) A margin balancing control (MBC) is proposed to optimize unbalanced stability margins. The system stability can be enhanced as the worst stability margin is improved. A design guideline is developed to determine the optimal control parameter. The validity of the MBC is investigated with both simulations and experiments.

The rest of this article is organized as follows. Section II introduces different representations of three-phase systems. Impedance models (IMs) are developed based on transfer matrices to analyze the harmonic stability. Section III investigates unbalanced stability margins affected by different factors analytically. As the system stability is limited by the worst factor, the MBC is proposed in Section IV to increase the worst stability margin. Following the developed design procedure, the MBC is designed and implemented for a 2-MW photovoltaic(PV) inverter system. To further investigate the validity of the MBC, simulations and experiments are conducted in Section V based on a down-scale prototype. Finally, the conclusion is drawn in Section VI. Derivations of IMs are provided in the Appendix.

II. Modeling and Harmonic Stability Analysis of Grid-Tied Inverter Systems

In this section, different representations of three-phase systems are introduced and compared with a focus of application fields. Among them, the transfer matrix is adopted to develop IMs, to investigate the harmonic stability.

A. Representation of Three-Phase Systems

A set of three-phase quantities $u_{abc} = \{u_a, u_b, u_c\}$ can be transformed equivalently to two-phase quantities in either stationary reference frames with Clark transformation or synchronous reference frames (SRF) with Park transformation. The latter is given in the following, which leads to a complex space vector with ω_g as the grid angular frequency [1]

$$\underline{u} = u_d + ju_q = \frac{2e^{\omega_g t}}{3}\left(u_a + e^{j\frac{2\pi}{3}}u_b + e^{j\frac{4\pi}{3}}u_c\right). \quad (1)$$

1) Complex Transfer Functions: For symmetric three-phase systems, which are featured with symmetric plants and control structures between the dq-axis in the SRF, the dynamics between input and output vectors $\underline{u}$ and $\underline{y}$ are described by complex transfer functions as given in (2). The 2-D MIMO system is further simplified in a one-dimensional complex SISO system. Complex transfer functions extend the modeling and analyses of converter systems to the negative-frequency domain [4]–[6], [14]–[16]. However, to model an asymmetric three-phase system, a second complex transfer function is needed [9], which leads to a MIMO system

$$\underline{y} = \underline{G}(s)\underline{u} \quad (2)$$

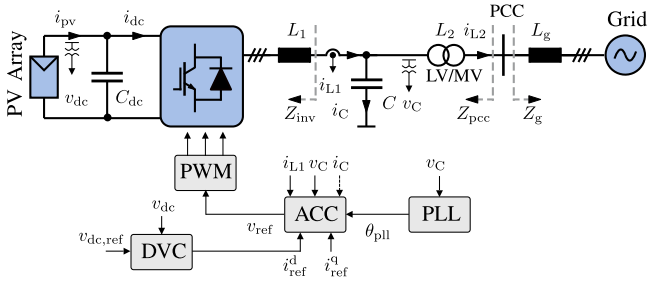

Fig. 1. System configuration of a three-phase PV inverter.

$$\underline{G}(s) = G_d(s) + jG_q(s). \tag{3}$$

2) Transfer Matrices: For asymmetric systems, either the plants or the control structures between the dq-axis are nonidentical. Complex space vectors are converted to real-space vectors, i.e., $\underline{u} \rightarrow u = [u_d, u_q]^T$, to facilitate the modeling with transfer matrices as given in (4). By means of that, the system dynamics can be described by a 2-D matrix as given in (5), where $G_{dd}(s)$, $G_{dq}(s)$, $G_{qd}(s)$, and $G_{qq}(s)$ are all real transfer functions. Asymmetric systems are featured with nonidentical diagonal elements, i.e., $G_{dd}(s) \neq G_{qq}(s)$. The cross-coupling effect between the dq-axis is described by off-diagonal elements $G_{qd}(s)$ and $G_{dq}(s)$. A complex transfer function is the special format of a transfer matrix if $G_{dd}(s) = G_{qq}(s) = G_d$ and $G_{dq}(s) = -G_{qd}(s) = G_q$

$$y = G(s)u \tag{4}$$

$$G(s) = \begin{bmatrix} G_{dd}(s) & -G_{qd}(s) \\ G_{dq}(s) & G_{qq}(s) \end{bmatrix}. \tag{5}$$

To investigate grid-tied inverter systems with asymmetric control loops, i.e., PLL and DVC, IMs are often used to describe the system dynamics [7], [8], which are also transfer matrices.

B. IM and Stability Analysis

The three-phase grid-tied PV inverter shown in Fig. 1 is considered for the analysis. An LCL filter is implemented for the harmonic suppression, where L_2 is realized by the leakage inductance of a step-up transformer. The ACC is implemented as the inner control loop considering the voltage feedforward filter and active damping. The capacitor voltages in the LCL filter are measured for the grid synchronization with an SRF-based PLL, The DVC is implemented to remain a constant dc-link voltage. The delay caused by the digital control and pulsewidth modulation (PWM) is also considered. An IM is developed by authors for the investigated system as presented in [22]. The stability can be assessed by applying the general Nyquist criterion to the impedance ratio as given in (6) [23], where Z_{pcc} and Z_g represent the inverter-side and the grid-side impedance at the point of common coupling (PCC), as marked in Fig. 1. The impedance Z_{pcc} is acquired by combining the inverter output impedance Z_{inv} and the filter parameters as given in (7), where Y_C and Z_{L2} are the capacitor admittance and the inductor impedance of the LCL filter. The inverter output impedance Z_{inv} is calculated according to the small-signal relationship of ac-side currents and voltages. Derivations of the developed IM are provided in the Appendix. To investigate the system stability, eigenvalues λ are calculated by solving the determinant given in (8). As IMs are developed with 2-D matrices, two eigenvalues are acquired. Nyquist curves are polar plots of eigenvalues. The system remains stable if no Nyquist curve encircles the point $(-1, j0)$

$$T = Z_{\text{pcc}}^{-1} Z_g \tag{6}$$

$$Z_{\text{pcc}} = (Z_{\text{inv}}^{-1} + Y_C)^{-1} + Z_{L2} \tag{7}$$

$$|T - \lambda I| = 0. \tag{8}$$

III. Unbalanced Stability Margins

The stability of three-phase grid-tied inverter systems depends on Nyquist curves of two eigenvalues. The two eigenvalues are usually different, which leads to unbalances stability margins. In this section, the reason for unbalanced stability margins is explained. The impact of control loops and operating conditions on the stability margin is investigated.

A. Stability Phase Margins of MIMO Systems

The stability margin is well defined for SISO systems [13]. However, a clear definition of the stability margin for MIMO systems is still under discussion [21]. Definitions of the PM and the gain margin for MIMO systems are proposed in [24] and [25] utilizing singular values of open-loop transfer matrices. However, the concept of singular values is not intuitive.

Gershgorin theorem is a more intuitive way to judge the stability of MIMO systems with geometrical interpretations [21]. The theorem applies to stability analyses for power electronic systems using the impedance ratio matrices [26], [27]. Although gain margins can be quantitatively evaluated, methods to improve stability margins are not discussed.

The generalized Nyquist criterion provides an intuitive approach for stability investigation similar to SISO systems [28]. It is employed in [29] to analyze the harmonic stability of power electronic systems utilizing the characteristic loci of the impedance ratio matrices. However, a strict concept of stability margins is missing to facilitate quantitative analyses and designs of MIMO systems. Therefore, a new definition of the stability PM for MIMO systems is proposed as follows based on the generalized Nyquist criterion.

Nyquist plots of the investigated system are depicted in Fig. 2. There are two Nyquist curves that are characteristic loci of eigenvalues acquired by 2-D matrices. As Nyquist plots are symmetric in the positive and the negative frequency range, only the curves in the positive frequency range are depicted. The Nyquist curve of two eigenvalue λ_i $(i = 1, 2)$ intersects the unit circle m $(m = 1, 2, \ldots)$ times. Each intersection has a phase difference φ_i^m to the point (-1.0), which leads to a PM as defined in (9). The PM of individual eigenvalues is determined by the minimum one as given in (10). As the system remains stable if no Nyquist curve encircles the point $(-1, j0)$, the minimum PM of two eigenvalues is considered as the PM of the overall system as defined in (11). The proposed definition of

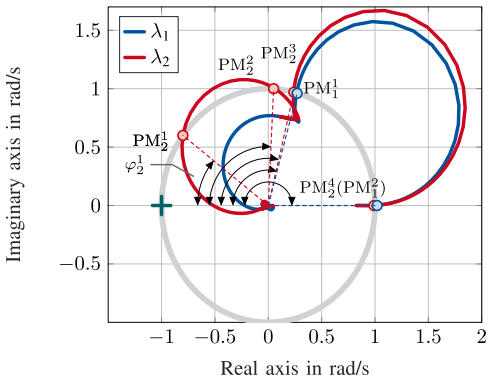

Fig. 2. Stability margin definition of a MIMO system

PMs facilitates quantitative analyses and designs of 2-D MIMO systems, which applies to general MIMO systems as well

$$\mathrm{PM}_i^m = 180^\circ - \varphi_i^m \tag{9}$$

$$\mathrm{PM}_i = \min\{\mathrm{PM}_i^m\} \tag{10}$$

$$\mathrm{PM}_{\mathrm{sys}} = \min\{\mathrm{PM}_1, \mathrm{PM}_2\}. \tag{11}$$

B. Mathematical Proof of Unbalanced Stability Margins

To explain the reason for unequal stability margins between the two Nyquist curves in 2-D systems, a mathematical proof is given as follows. The frequency-domain expression of two eigenvalues is derived in (12), which is calculated according to (8), considering that the impedance ratio matrix T is in format of (5). It is found that:

1) two eigenvalues are nonidentical, i.e., $\lambda_1(j\omega) \neq \lambda_2(j\omega)$, if either diagonal elements $G_{dd}(j\omega)$ and $G_{qq}(j\omega)$ are not equal, or off-diagonal elements $G_{dq}(j\omega)$ and $G_{qd}(j\omega)$ are nonzero values;
2) two eigenvalues are mirror-symmetric in positive and negative frequency ranges, i.e., $\lambda_{1,2}(j\omega) = \lambda_{1,2}^*(-j\omega)$

$$\begin{aligned}\lambda_{1,2}(j\omega) &= \frac{G_{dd}(j\omega)+G_{qq}(j\omega)}{2} \\ &\quad \pm \sqrt{\left(\tfrac{G_{dd}(j\omega)-G_{qq}(j\omega)}{2}\right)^2 + G_{dq}(j\omega)G_{qd}(j\omega)} \\ &= \frac{G_{dd}^*(-j\omega)+G_{qq}^*(-j\omega)}{2} \\ &\quad \pm \sqrt{\left(\tfrac{G_{dd}^*(-j\omega)-G_{qq}^*(-j\omega)}{2}\right)^2 + G_{dq}^*(-j\omega)G_{qd}^*(-j\omega)} \\ &= \lambda_{1,2}^*(-j\omega). \end{aligned} \tag{12}$$

Due to the implementation of asymmetric control loops, e.g., the PLL and DVC, diagonal elements are unequal according to expressions (25)–(30) in the Appendix. Due to the delay effect caused by digital control and nonideal cross-coupling compensations, off-diagonal elements are usually nonzero values. As a result, it is inevitable to have nonidentical eigenvalues, which leads to unbalanced PMs. Different to symmetric three-phase systems described by complex transfer functions, in which unbalanced PMs are observed between the positive and the negative frequency range, asymmetric three-phase systems have unbalanced PMs between two Nyquist curves.

TABLE I
SYSTEM AND CONTROL PARAMETERS OF 2-MW SYSTEM

Parameter	Value	Parameter	Value
$V_{\mathrm{g,ll}}^{\mathrm{rms}}$	550 V	P_{n}	2 MW
f_{sw}	3 kHz	f_{sp}	6 kHz
V_{dc}	1200 V	f_{g}	50 Hz
C_{dc}	15 mF	L_1	120 µH
C	1 mF	L_2	40 µH
$f_{\mathrm{bw}}^{\mathrm{ACC}}$	300 Hz	$K_{\mathrm{p}}^{\mathrm{ACC}}$	0.23 Ω
$f_{\mathrm{bw}}^{\mathrm{PLL}}$	30 Hz	$K_{\mathrm{p}}^{\mathrm{PLL}}$	0.36 rad/sV
$f_{\mathrm{bw}}^{\mathrm{DVC}}$	20 Hz	$K_{\mathrm{p}}^{\mathrm{DVC}}$	3.6 S

C. Impact of Control Loops and Operating Conditions

To further analyze the cause and the impact of unbalanced stability margins, the impact of different control loops and operating conditions is investigated for a 2-MW PV inverter specified in Table I. To reveal the adverse influence of unbalanced PMs obviously, the analyses are based on a weak-grid condition with the short-circuit ratio SCR = 3.

1) Control Delay: Due to the implementation of digital control and the latching effect of PWM, a delay T_{del} is inevitable between the control command and inverter output voltage. For the double-update PWM, a delay of $T_{\mathrm{del}} = 1.5\,T_{\mathrm{sp}}$ with the sampling time T_{sp} should be considered [14]. Nyquist curves considering different control delays are depicted in Fig. 3(a). For the ideal case without time delay, i.e., $T_{\mathrm{del}} = 0$, the cross-coupling terms in off-diagonal elements can be compensated by the decoupling terms. As a result, quasi-identical Nyquist curves are observed. If a normal control delay $T_{\mathrm{del}} = 1.5\,T_{\mathrm{sp}}$ is considered, an imbalance between two Nyquist curves is induced. However, the system PM $\mathrm{PM}_{\mathrm{sys}}$ is not influenced. If the delay time further increases, the imbalance becomes larger, and the PM of both eigenvalues decreases simultaneously, which leads to a reduction of $\mathrm{PM}_{\mathrm{sys}}$.

2) Alternating-Current Control: The impact of different ACC bandwidths $f_{\mathrm{bw}}^{\mathrm{ACC}}$ on stability margins is illustrated in Fig. 3(b). With an increased ACC bandwidth, the PM of both Nyquist curves decreases. However, the imbalance between two eigenvalues is reduced, as two Nyquist curves become closer to each other.

3) Phase-Locked Loop: The Nyquist curves influenced by different PLL bandwidths $f_{\mathrm{bw}}^{\mathrm{PLL}}$ are presented in Fig. 3(c). With an increased PLL bandwidth, the PM of both Nyquist curves decreases significantly, which easily leads to instabilities. The reason is that the negative-resistance region induced by the PLL extends toward high-frequency regions with an increased bandwidth [22]. The imbalance between the two PMs increases simultaneously with a higher bandwidth.

4) Direct-Voltage Control Loop: The Nyquist curves influenced by different DVC bandwidths $f_{\mathrm{bw}}^{\mathrm{DVC}}$ are presented in

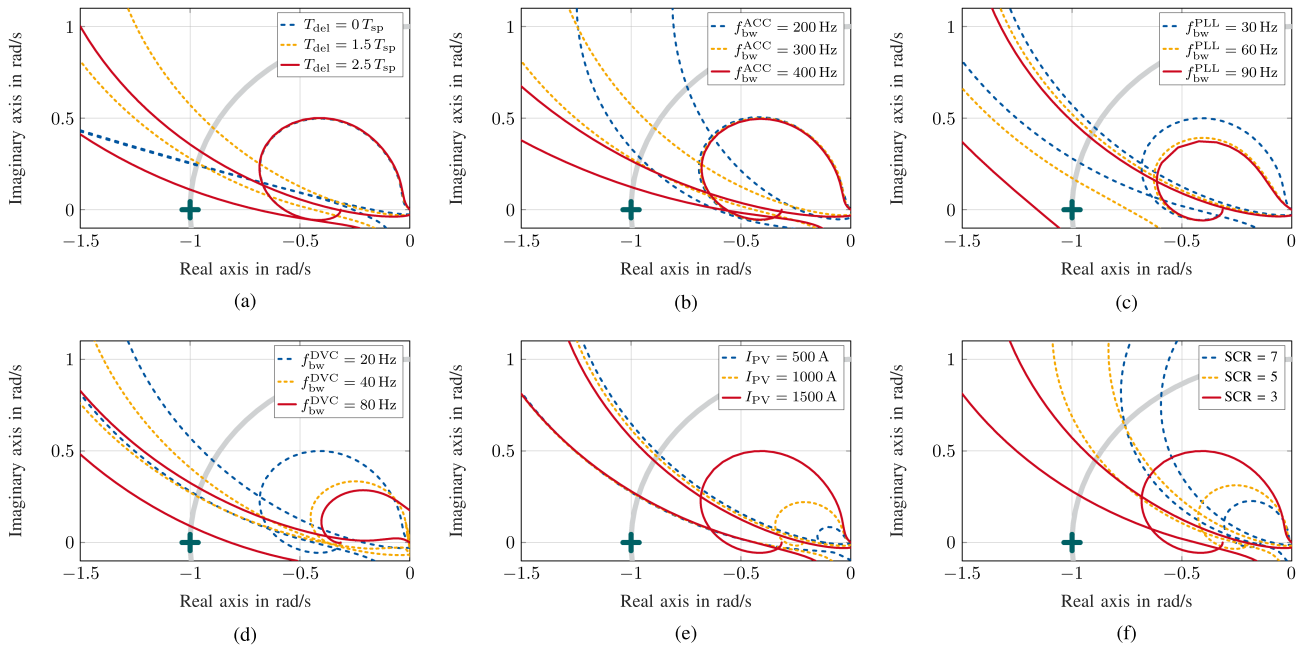

Fig. 3. Unbalanced stability margins influenced by different factors. (a) Impact of the control delay. (b) Impact of $f_{\mathrm{bw}}^{\mathrm{ACC}}$. (c) Impact of $f_{\mathrm{bw}}^{\mathrm{PLL}}$. (d) Impact of $f_{\mathrm{bw}}^{\mathrm{DVC}}$. (e) Impact of I_{pv}. (f) Impact of SCR.

Fig. 3(d). With an increased DVC bandwidth from 20 to 40 Hz, though one of the Nyquist curves decreases significantly, the worst PM is not influenced, which indicates the possibility to optimize the DVC bandwidth within this range. If the DVC bandwidth further increases, both PMs decrease, and the imbalance between two PMs increases as well.

5) PV Current: The impact of different PV currents I_{pv} on Nyquist curves is illustrated in Fig. 3(e). With an increased PV current from 500 to 1500 A, the worst PM remains unchanged, while the other PM decreases slightly. It can be, thus, concluded that the system PM $\mathrm{PM_{sys}}$ is almost independent of the PV current.

6) Grid Stiffness: The Nyquist curves influenced by different grid impedances are shown in Fig. 3(f). A higher grid impedance (lower SCR) reduces the PM of both Nyquist curves, leading to a rapid decrease of $\mathrm{PM_{sys}}$. The worst PM is clearly the performance barrier for weak-grid operations.

In summary, unbalanced stability margins are inevitable due to the control delay, cross-coupling effects, and asymmetric control loops. Different operating currents and a normal control delay do not affect $\mathrm{PM_{sys}}$. Among different factors, the PLL has the most significant influence on both PMs and the imbalance between them. To improve the system stability especially for weak-grid operations, the worst stability margin mainly influenced by control loops should be compensated.

IV. Margin Balancing Control

From the engineering point of view, it is difficult to achieve the best performance for all aspects in a system simultaneously. An optimal design is usually a tradeoff among different goals. If the worst stability margin can be improved by slightly reducing the best one, the overall system stability margin $\mathrm{PM_{sys}}$ can increase, which leads to the idea of the MBC.

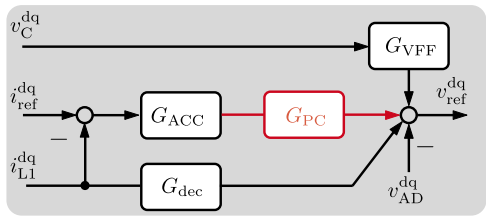

Fig. 4. Implementation of the PC.

A. Control Structure

According to Nyquist curves in Fig. 3(a), quasi-balanced PMs are acquired if no control delay is considered. Thus, the worst stability margin can be improved utilizing a similar structure of the delay compensation. A delay is essentially a rotation if represented by Euler's formula as given in (13). Hence, a rotation structure is considered to balanced two PMs, leading to the idea of the PC function G_{PC}. As the IM is developed with transfer matrices, G_{PC} is defined in format of a constant matrix as given in (14), where θ_{PC} is the PC angle. The PC function is implemented in the ACC after the PI controller as depicted in Fig. 4. Although the PC function adopts a similar structure of the delay compensation, it aims actually to improve the system PM $\mathrm{PM_{sys}}$ majorly influenced by asymmetric control loops, in order to enhance the system stability especially for weak-grid operations

$$G_{\mathrm{del}} = e^{-j\omega_g T_{\mathrm{del}}} = \cos\left(\omega_g T_{\mathrm{del}}\right) - j\sin\left(\omega_g T_{\mathrm{del}}\right) \quad (13)$$

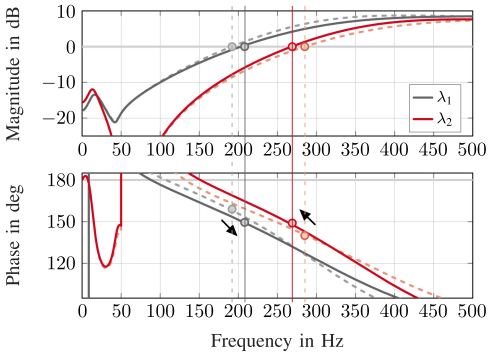

Fig. 5. Frequency responses influenced by G_{PC} (dashed lines: w/o G_{PC}; solid lines: w/G_{PC}).

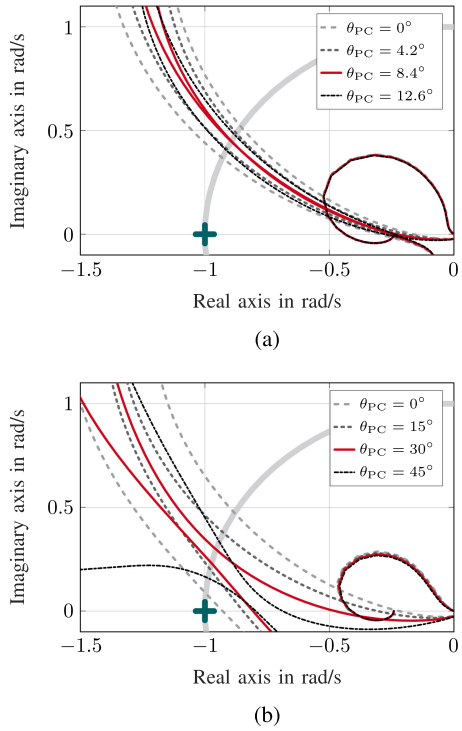

Fig. 6. Stability margins influenced by different θ_{PC}. (a) Low PLL bandwidth ($f_{\mathrm{bw}}^{\mathrm{PLL}} = 30$ Hz). (b) High PLL bandwidth ($f_{bw}^{\mathrm{PLL}} = 100$ Hz).

$$G_{\mathrm{PC}}(\theta_{\mathrm{PC}}) = \begin{bmatrix} \cos(\theta_{\mathrm{PC}}) & -\sin(\theta_{\mathrm{PC}}) \\ \sin(\theta_{\mathrm{PC}}) & \cos(\theta_{\mathrm{PC}}) \end{bmatrix}. \tag{14}$$

The effect of the PC function is first observed in Fig. 5 with the frequency response of two eigenvalues considering a normal grid condition with SCR $= 4$. The implemented G_{PC} has almost no influence on the shape of frequency responses. However, it can rotate both the magnitudes and the phases of two eigenvalues toward opposite directions. As a result, the stability margins of two eigenvalues become more balanced. This improvement is especially crucial for weak-grid operations, as the worst PM acts as the performance barrier as indicated in Fig. 3. To intuitively investigate the defined PMs influenced by different θ_{PC}, The Nyquist curves of two eigenvalues are observed in Fig. 6 considering SCR $= 4$. Ideally, balanced stability margins are preferred, as the system PM $\mathrm{PM}_{\mathrm{sys}}$ can achieve the maximum value, as indicated in Fig. 6(a). However, this cannot be realized in some cases, e.g., with a high PLL bandwidth. The worst PM starts to decrease again before two Nyquist curves having the same PM, as shown in Fig. 6(b). A too high value of θ_{PC} should be avoided to prevent the overcorrection, which can reduce $\mathrm{PM}_{\mathrm{sys}}$ as observed in both cases. To guarantee the optimal design considering various cases, a generalized design procedure is developed.

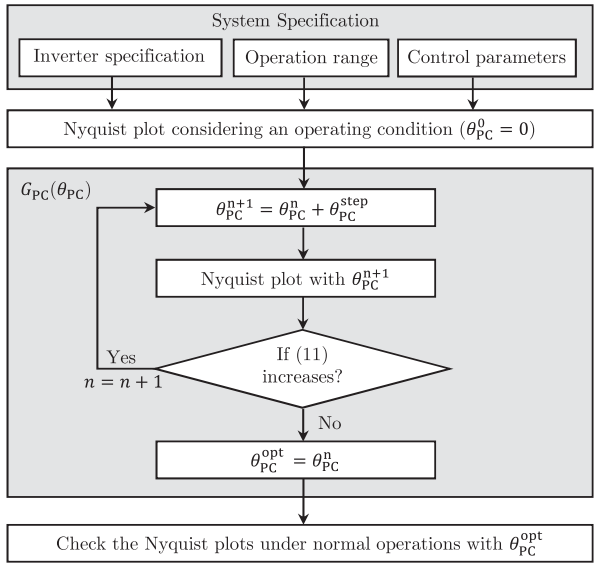

Fig. 7. Design flowchart of MBC.

B. Design Procedure

To determine the PC angle θ_{PC} when implementing the MBC, a design procedure is developed based on the graphical approach as shown in Fig. 7. Nyquist curves are depicted for the investigated system considering a specific operating condition. Hereinafter, the MBC is implemented starting from $\theta_{\mathrm{PC}} = 0$. The PC angle increases step by step, and Nyquist curves are observed in each step. An optimal design for this operating condition is obtained if the system PM $\mathrm{PM}_{\mathrm{sys}}$ defined in (11) achieves the maximum value. In special cases, two Nyquist curves can intersect with the unit circle at the same point, which leads to exactly balanced stability margins as described in (15). To facilitate the design, θ_{PC} is characterized in a per unit value represented by the PC factor K_{PC} as defined in (16), which is in relation to the minimum time interval in the system, i.e., the sampling time T_{sp}. For the motor drive application in [14], the implemented PC angle is determined equivalently as $K_{\mathrm{PC}} = 1.5$, which compensates unbalanced PMs in positive and negative frequencies caused by the control delay $T_{\mathrm{del}} = 1.5\,T_{\mathrm{sp}}$. However, a higher value of K_{PC} is required in this work to compensate unbalanced PMs influenced by asymmetric control loops especially the PLL, to enhance the harmonic stability for weak-grid operations. It is suggested to set the increment step $\theta_{\mathrm{PC}}^{\mathrm{step}}$ as (17) to obtain a satisfied design. For high-power converters with a large sampling time T_{sp}, a smaller increment

TABLE II
COMPARISON OF DIFFERENT METHODS TO BALANCE UNEQUAL STABILITY MARGINS

Reference	Modeling Approach	Considered Impacts	Unbalanced PMs	Design Guideline	Stability Issue
[14]	Complex vector of the open-loop transfer function	ACC, delay	$PM_+ \neq PM_-$	$\theta_{PC} = 1.5\,\omega_g T_{sp}$	Controller stability
[15]	Complex vector of the open-loop transfer function	ACC, delay	$PM_+ \neq PM_-$	$\theta_{PC} = \lvert PM_+ - PM_- \rvert/2$	Controller stability
Proposed	Transfer matrix of the impedance return ratio	ACC, delay, PLL, DVC, L_g, I_{pv}	$PM_1 \neq PM_2$	Maximize PM_{sys}	Harmonic stability

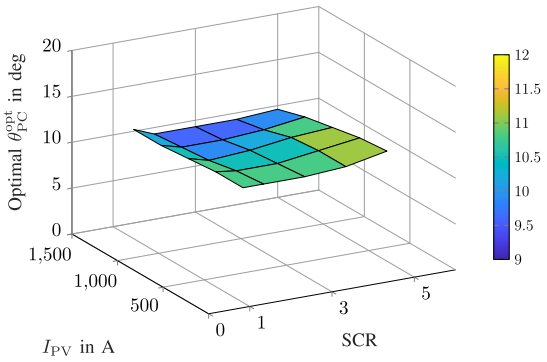

Fig. 8. Optimal PC angle for different operation conditions.

step is preferred to determine the parameter more accurately

$$PM_1 = PM_2 = PM_{sys} \tag{15}$$

$$\theta_{PC} = K_{PC}\,\omega_g T_{sp} \cdot \frac{180^\circ}{\pi} \tag{16}$$

$$\Theta_{PC}^{step} = \omega_g T_{sp} \cdot \frac{180^\circ}{\pi}. \tag{17}$$

C. Design Case

A design case is presented based on the investigated 2-MW PV inverter system specified in Table I. The optimal PC angle θ_{PC}^{opt} is designed for stable operations considering an increment step $\theta_{PC}^{step} = 0.1\,\Theta_{PC}^{step} = 0.3^\circ$. The overall variation of θ_{PC}^{opt} is in the range of $9.3^\circ - 12^\circ$ ($K_{PC} = 3.1 - 4.0$), which indicates that the optimal design is almost independent of operating conditions. It is recommended to consider the minimum value of θ_{PC}^{opt} as the global optimal design Θ_{PC}^{opt}, in order to prevent the overcorrection in wide operation ranges. An overcorrection reduces PM_{sys}, as shown in Fig. 6, which can lead to poor performances as validated in experiments.

To investigate the validity of the MBC, the stability boundary of the grid stiffness is analyzed. The system loses stability for the operation with $I_{pv} = 1000$ A and $L_g = 300\,\mu$H (SCR $= 1.6$), as shown in Fig. 9. Unbalanced PMs can be observed in the Nyquist plot, i.e., $PM_1 = 12^\circ$ and $PM_2 = 0.5^\circ$. By implementing the MBC with the global optimal design $\Theta_{PC}^{opt} = 9.3^\circ$ obtained from Fig. 8, quasi-balanced PMs are acquired with $PM_1 = 6^\circ$ and $PM_2 = 5.5^\circ$. As a result, the system can remain stable even with a higher grid impedance as validated in Fig. 9(b). The stability boundary after implementing the MBC increases to $L_g = 350\,\mu$H (SCR $= 1.4$), which accounts for 17% improvement.

The proposed MBC can improve not only the system stability, but also the transient performance in normal operations. Considering a stable operation with $L_g = 190\,\mu$H (SCR $= 2.5$).

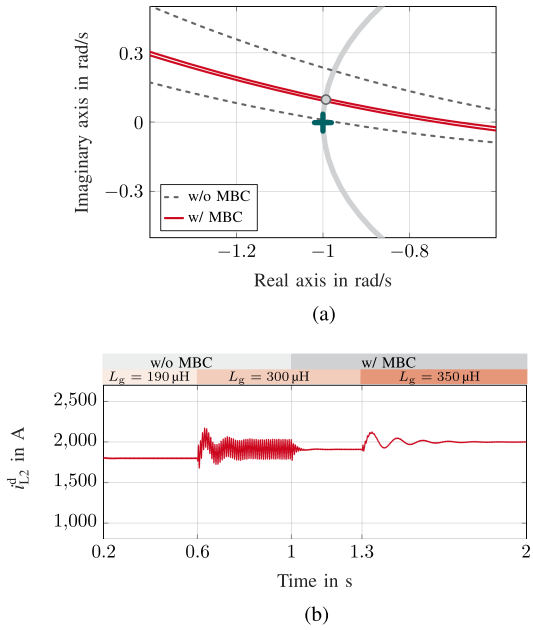

Fig. 9. Validation of the MBC. (a) Nyquist plots ($L_g = 300\,\mu$H). (b) Simulation result.

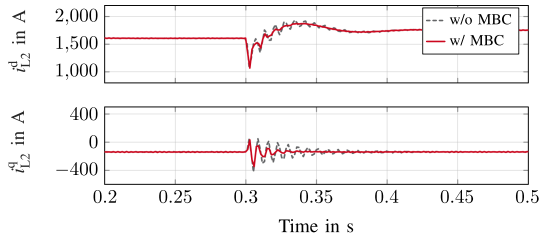

Fig. 10. Comparison of transient performances.

The transient waveforms for a step change of the PV current are observed in Fig. 10. Resonances occur in transients due to the small PM_{sys}. After implementing the MBC, the transient performance is improved.

The proposed MBC is compared to other methods dealing with unbalanced stability margins as summarized in Table II. Previous studies, e.g., [14], [15], utilize the complex vector of the open-loop transfer function to investigate unbalanced stability margins between positive and negative frequency domains. While this work utilizes the impedance return ratio matrix to analyze unbalanced stability margins between two eigenvalues, which is able to take the impact of asymmetric control structures and operating conditions into account. Moreover, the design presented in [14] compensates only the delay effect. The design rule suggested in [15] may not always be effective, as the sum of two PMs variates after implementing the MBC as presented

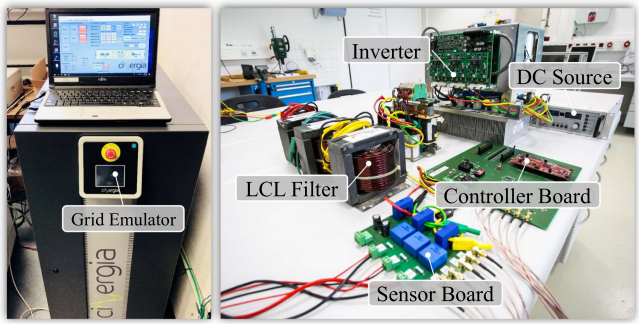

Fig. 11. Experimental setup.

TABLE III
SYSTEM AND CONTROL PARAMETERS OF 1-kW SYSTEM

Parameter	Value	Parameter	Value
$V_{\mathrm{g,ll}}^{\mathrm{rms}}$	90 V	P_{n}	1 kW
f_{sw}	10 kHz	f_{sp}	20 kHz
V_{dc}	180 V	f_{g}	50 Hz
C	10 µF	L_1	2.5 mH
$f_{\mathrm{bw}}^{\mathrm{ACC}}$	1 kHz	$K_{\mathrm{p}}^{\mathrm{ACC}}$	16 Ω
$f_{\mathrm{bw}}^{\mathrm{PLL}}$	30 Hz	$K_{\mathrm{p}}^{\mathrm{PLL}}$	2.3 rad/sV

TABLE IV
EXPERIMENT SCENARIOS

Cases	$i_{\mathrm{ref}}^{\mathrm{d}}$ (A)	$f_{\mathrm{bw}}^{\mathrm{PLL}}$ (Hz)	L_{g} (mH)	PF	θ_{PC}
Case 1	10	30	$9-14.5$	Unity	12.6°
Case 2	$2\rightarrow 6$	170	3.5	Unity	$0°-21.6°$
Case 3	10	90	5.5	Unity	14.4°
Case 4	10	170	3.5	Unity	14.4°
Case 5	6	230	3.5	$0.89-0.83$	14.4°

in Fig. 9. The reason is that asymmetric control loops introduce nonlinearity in systems, which cannot guarantee an equal change in two stability margins as also indicated in Fig. 6(b). The proposed design guideline combining the graphical approach provides a more general criterion. It should be noticed that the work in [14] and [15] aims to deal with the controller stability influenced by the control delay and the cross-coupling effect, while the proposed MBC aims to cope with the harmonic stability, which is strongly affected by the PLL and the grid stiffness. Notice that the impedance-shaping control in [19] and [20] improves the harmonic stability by introducing an "external force," which shapes the frequency responses with an additional control loop. While the MBC enhances the harmonic stability by optimizing the system "internal imbalance," which only rotates the frequency responses, as shown in Fig. 5. Although it is possible to increase both PMs simultaneously with the impedance-shaping methods, the MBC is compatible to other methods to further optimize the system, as long as unbalanced PMs exist. As a summary, the proposed MBC features following advantages.

1) The worst stability margin in a system, which acts as the performance barrier, can be improved without affecting other loops.

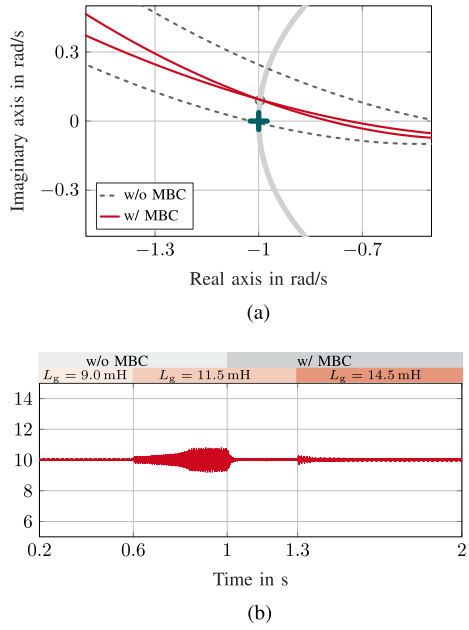

Fig. 12. Validation of case 1. (a) Nyquist plots ($L_g = 115$ mH). (b) Simulation result.

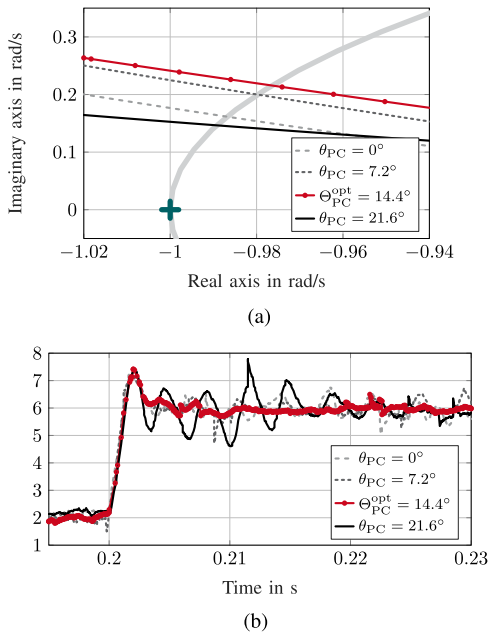

Fig. 13. Validation of case 2. (a) Nyquist plots ($\hat{i}_{L2}^{d} = 6$ A). (b) Experiment results.

2) The MBC is implemented in the ACC, which requires no additional measurements and feedbacks.
3) The design is almost independent of the operating current, which is effective for a wide operating range.

V. SIMULATION AND EXPERIMENTAL VALIDATION

The validity of the proposed MBC is further investigated based on a 1-kW prototype. As shown in Fig. 11, the test setup is comprised of a three-phase inverter, a grid emulator, a dc voltage source, the control and sensor circuit boards as

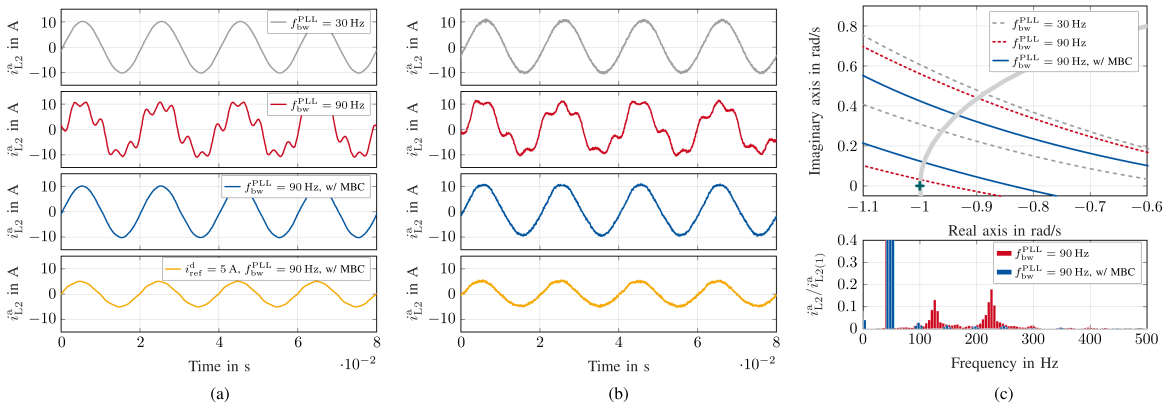

Fig. 14. Validation of case 3. (a) Simulation results. (b) Experiment results. (c) Nyquist curves and resonance spectrum.

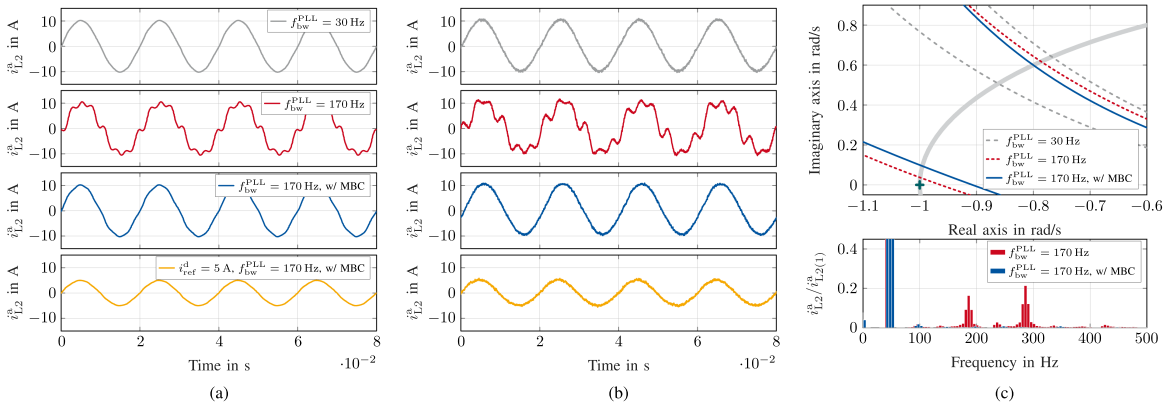

Fig. 15. Validation of case 4. (a) Simulation results. (b) Experiment results. (c) Nyquist curves and resonance spectrum.

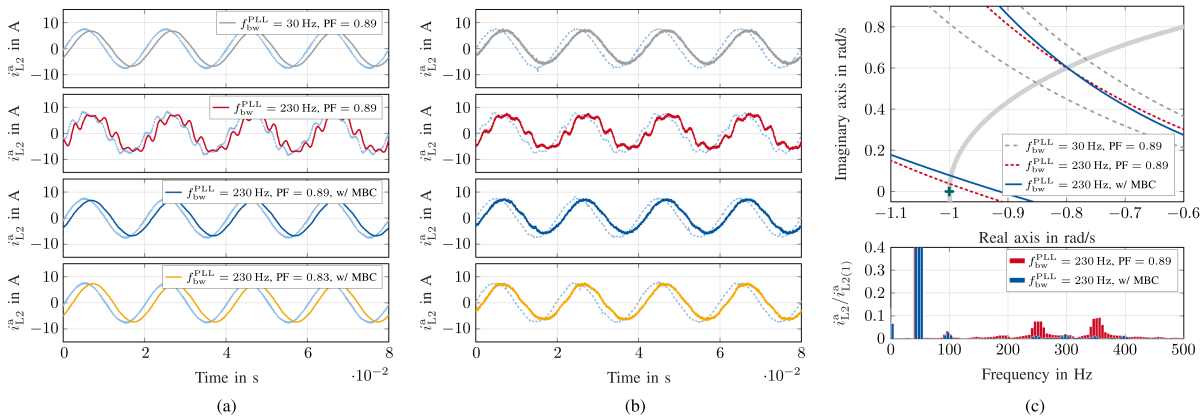

Fig. 16. Validation of case 5 (dotted line: phase voltage of v_C^a). (a) Simulation results. (b) Experiment results. (c) Nyquist curves and resonance spectrum.

well as LCL filters. The system and control parameters for the down-scale test setup are specified in Table III. As no DVC is implemented, the simplified IM without the DVC is utilized for the analyses as derived in the Appendix. Based on the design procedure proposed in Fig. 7, the PC angle of the MBC is designed for the prototype considering an increment step $\theta_{\text{PC}}^{\text{step}} = \Theta_{\text{PC}}^{\text{step}} = 0.9°$. Five different scenarios are considered for validations as specified in Table IV.

A. Case 1

Case 1 investigates the stability boundary of the grid stiffness with a normal PLL bandwidth $f_{\text{bw}}^{\text{PLL}} = 30\,\text{Hz}$. Due to the limited filter components available in the laboratory, case 1 is presented with simulations. The system loses stability if the grid impedance increases to $L_g = 11.5\,\text{mH}$ (SCR $= 1.9$). The worst PM is the performance barrier, as seen in Fig. 12(a). After implementing the MBC, balanced PMs are observed and PM_{sys}

is improved. As a result, the system can remain stable for a weaker grid until $L_g = 14.5$ mH (SCR $= 1.5$), which accounts for 26% improvement. The analyses is validated in simulations as depicted in Fig. 12(b).

B. Case 2

Case 2 validates the necessity to optimally design the PC angle when implementing the MBC. The step response is observed with different PC angles from 0° to 21.6°. To clearly compare transient performances, the PLL bandwidth is increased to 170 Hz, which intentionally reduces the PM of all Nyquist curves as depicted in Fig. 3(c). Due to the high PLL bandwidth, exactly balanced PMs cannot be obtained as explained in Fig. 6(b). Hence, the optimal design is obtained by maximizing the system PM PM_{sys}. Compared to case 1 with a normal PLL bandwidth, a slightly higher PC angle is required to maximize the worst PM for operations with a high PLL bandwidth, as also observed in Fig. 6. A poor transient is observed in the step response if no MBC is implemented, as shown in Fig. 13. The reason is that the system PM PM_{sys} is close to the point $(-1, j0)$. If the MBC is implemented with $\theta_{\text{PC}} = 7.2°$, PM_{sys} increases and the transient performance is improved. If the PC angle increases to the optimal design $\Theta_{\text{PC}}^{\text{opt}} = 14.4°$, the maximum value of PM_{sys} is obtained, so that a better performance is achieved. If the PC angle further increases to $\theta_{\text{PC}} = 21.6°$, PM_{sys} decreases due to the overcorrection, which leads to a worse performance. As a result, significant resonances are observed in the transient. Both Nyquist curves and experimental results indicate that the MBC with the optimal design improves the system PM PM_{sys} to the highest value, which can maximally extend the stability boundary.

C. Case 3

Case 3 validates the stability boundary of the PLL bandwidth with the grid impedance $L_g = 5.5$ mH (SCR $= 4.1$). The system remains stable with a normal PLL bandwidth. If the PLL bandwidth is intentionally increased to $f_{\text{bw}}^{\text{PLL}} = 90$ Hz, the imbalance between two PMs increases and the worst PM becomes close to the point $(-1, j0)$, which limits the system PM PM_{sys}. As a result, resonances appear as observed in both simulations and experiments in Fig. 14. The stability margin PM_{sys} increases if the MBC is implemented, so that the system can remain stable again. Although it is impossible to achieve exactly balanced PMs due to the high PLL bandwidth, the stability boundary of the PLL bandwidth can be extended from 90 to 100 Hz with the improved system PM PM_{sys} after implementing the MBC, which accounts for 11% improvement. The MBC applies to the operation with a low injection current as well.

D. Case 4

Case 4 validates the stability boundary of the PLL bandwidth considering $L_g = 3.5$ mH (SCR $= 6.5$). The system loses stability if the PLL bandwidth is increased to $f_{\text{bw}}^{\text{PLL}} = 170$ Hz. Resonances are observed in simulations and experiments as illustrated in Fig. 15(a) and (b). Nyquist curves indicate the increase of the PM imbalance and the decrease of the system PM PM_{sys}, as presented in Fig. 15(c). After implementing the MBC with the designed parameter, PM_{sys} can be improved and the resonances vanish. The MBC is valid for small current injections as well. Notice that the resonances in case 4 are featured with higher frequencies compared to the ones in case 3. The reason is that the negative-resistance effect induced by the PLL extends toward high-frequency regions with an increased bandwidth [22], which also shifts the resonances toward high-frequency ranges.

E. Case 5

Case 5 validates the stability boundary of the PLL bandwidth considering a nonunity power factor, as grid-tied inverters are supposed to operate with a certain amount of reactive current with the power factor PF ≥ 0.85 in normal operations according to the grid code [30]. Considering an operation with $L_g = 3.5$ mH and PF $= 0.89$, resonances occur if the PLL bandwidth increases to $f_{\text{bw}}^{\text{PLL}} = 230$ Hz, which is validated with simulations and experiments as depicted in Fig. 16. The system becomes stable if the MBC is implemented, which is even valid for the operation with PF $= 0.83$. Nyquist plots considering the operation with PF $= 0.89$ are depicted in Fig. 16(c). It is observed in Nyquist curves that, the system PM PM_{sys} is improved after activating the MBC.

VI. Conclusion

This article investigates unbalanced stability margins for a three-phase grid-tied PV inverter system based on the proposed definition of system PMs. It is found that the implemented asymmetric control loops increase the system "internal imbalance," leading to unbalance stability margins. The worst stability margin acts as the performance barrier, which can induce harmonic instabilities especially in weak-grid conditions. To enhance the system stability, the MBC is proposed to improve the worst stability margin by optimizing the system "internal imbalance." A design approach is developed to determine the control parameter. The validity of the MBC is investigated with both simulations and experiments for different scenarios.

Appendix
Transfer Matrices in IM

Derivations of IM and related transfer matrices are given as follows. For clarity real vectors are represented with $x^{dq} = [x^d, x^q]^T$, a small-signal variable is presented with $\hat{x}$, while a steady-state value is described with X. To precisely describe the influence of the PLL, two reference frames are required, which are noted with the superscript c for the control frame and the superscript s for the system frame.

1) Alternating-Current Control: The dynamic equation of the ACC is given in (18), where m is the modulation index, i_{ref} is the reference current. i_{L1}, i_C, and v_C are the measured currents and voltage in the LCL filter. G_{ACC} represents the control matrix of the ACC with the PI controller $F_{\text{ACC}} = K_p^{\text{ACC}} + /sK_i^{\text{ACC}}s$ K_p^{ACC}. G_{dec} represents the decoupling transfer matrix, where w_g is the grid frequency. G_{VFF} is the transfer matrix of the voltage

feedforward filter, where $\omega_{\text{VFF}} = 2\pi f_{\text{bw}}^{\text{VFF}}$ is the filter bandwidth. G_{AD} is the transfer matrix of the active damping, where K_{AD} is the damping factor. G_{del} models the system delay with Pade approximation, where T_{del} includes in total $1.5\,T_{\text{sp}}$ considering the digital implementation of the double-update PWM

$$\begin{bmatrix} m^{d,c} \\ m^{q,c} \end{bmatrix} \frac{v_{\text{dc}}}{2} = G_{\text{del}} G_{\text{ACC}} \begin{bmatrix} i_{\text{ref}}^{d,c} \\ i_{\text{ref}}^{q,c} \end{bmatrix} - G_{\text{del}} \left(G_{\text{ACC}} + G_{\text{dec}} \right) \begin{bmatrix} i_{L1}^{d,c} \\ i_{L1}^{q,c} \end{bmatrix} + G_{\text{del}} G_{\text{VFF}} \begin{bmatrix} v_C^{d,c} \\ v_C^{q,c} \end{bmatrix} - G_{\text{del}} G_{\text{AD}} \begin{bmatrix} i_C^{d,c} \\ i_C^{d,c} \end{bmatrix} \tag{18}$$

$$G_{\text{ACC}} = \begin{bmatrix} F_{\text{ACC}} & 0 \\ 0 & F_{\text{ACC}} \end{bmatrix} \tag{19}$$

$$G_{\text{dec}} = \begin{bmatrix} 0 & \omega_g L_1 \\ -\omega_g L_1 & 0 \end{bmatrix} \tag{20}$$

$$G_{\text{VFF}} = \begin{bmatrix} \frac{\omega_{\text{VFF}}}{s+\omega_{\text{VFF}}} & 0 \\ 0 & \frac{\omega_{\text{VFF}}}{s+\omega_{\text{VFF}}} \end{bmatrix} \tag{21}$$

$$G_{\text{AD}} = \begin{bmatrix} K_{\text{AD}} & 0 \\ 0 & K_{\text{AD}} \end{bmatrix} \tag{22}$$

$$G_{\text{del}} = \begin{bmatrix} \frac{2-sT_{\text{del}}}{2+sT_{\text{del}}} & 0 \\ 0 & \frac{2-sT_{\text{del}}}{2+sT_{\text{del}}} \end{bmatrix}. \tag{23}$$

1) Phase-Locked Loop: The PLL influences the synchronization angle as shown in (24), which has a direct influence on the Park transformation. $F_{\text{PLL}} = K_p^{\text{PLL}} + /sK_i^{\text{PLL}}s$ is the PI controller of the PLL. When implementing Park transformations, variables such as i_{L1}, i_C, v_C need to be converted from the system to control frame, while the modulation command v_{ref} needs to be converted to the system frame serving as the modulator input. The small-signal relationship between control and system frames are given in (25)–(28). Notice that the PLL mainly influences q-axis elements in matrices, which can increase the imbalance between two eigenvalues

$$H_{\text{PLL}} = \frac{\hat{\theta}_{\text{pll}}}{\hat{v}_C^q} = \frac{F_{\text{PLL}}}{s + V_C^{d,s} F_{\text{PLL}}} \tag{24}$$

$$\begin{bmatrix} \hat{i}_{L1}^{d,c} \\ \hat{i}_{L1}^{q,c} \end{bmatrix} = \begin{bmatrix} \hat{i}_{L1}^{d,s} \\ \hat{i}_{L1}^{q,s} \end{bmatrix} + \underbrace{\begin{bmatrix} 0 & I_{L1}^{q,s} H_{\text{PLL}} \\ 0 & -I_{L1}^{d,s} H_{\text{PLL}} \end{bmatrix}}_{G_{\text{PLL}}^{i}} \begin{bmatrix} \hat{v}_C^{d,s} \\ \hat{v}_C^{q,s} \end{bmatrix} \tag{25}$$

$$\begin{bmatrix} \hat{i}_C^{d,c} \\ \hat{i}_C^{q,c} \end{bmatrix} = \begin{bmatrix} \hat{i}_C^{d,s} \\ \hat{i}_C^{q,s} \end{bmatrix} + \underbrace{\begin{bmatrix} 0 & I_C^{q,s} H_{\text{PLL}} \\ 0 & -I_C^{d,s} H_{\text{PLL}} \end{bmatrix}}_{G_{\text{PLL}}^{ic}} \begin{bmatrix} \hat{v}_C^{d,s} \\ \hat{v}_C^{q,s} \end{bmatrix} \tag{26}$$

$$\begin{bmatrix} \hat{v}_C^{d,c} \\ \hat{v}_C^{q,c} \end{bmatrix} = \begin{bmatrix} \hat{v}_C^{d,s} \\ \hat{v}_C^{q,s} \end{bmatrix} + \underbrace{\begin{bmatrix} 0 & V_C^{q,s} H_{\text{PLL}} \\ 0 & -V_C^{d,s} H_{\text{PLL}} \end{bmatrix}}_{G_{\text{PLL}}^{v}} \begin{bmatrix} \hat{v}_C^{d,s} \\ \hat{v}_C^{q,s} \end{bmatrix} \tag{27}$$

$$\begin{bmatrix} \hat{m}^{d,s} \\ \hat{m}^{q,s} \end{bmatrix} = \begin{bmatrix} \hat{m}^{d,c} \\ \hat{m}^{q,c} \end{bmatrix} + \underbrace{\begin{bmatrix} 0 & -M^{q,s} H_{\text{PLL}} \\ 0 & M^{d,s} H_{\text{PLL}} \end{bmatrix}}_{G_{\text{PLL}}^{m}} \begin{bmatrix} \hat{v}_C^{d,s} \\ \hat{v}_C^{q,s} \end{bmatrix}. \tag{28}$$

1) Direct-Voltage Control: The dynamic equation of the DVC is given in (29), which serves as an input of (18), where $F_{\text{DVC}} = K_p^{\text{DVC}} + /sK_i^{\text{DVC}}s$ is the PI controller of the DVC. The small-signal variable $\hat{v}_{\text{dc}}$ is influenced by both the modulation index m and ac-side current i_{L1} as given in (30) after linearization, where $Y_{\text{dc}} = sC_{\text{dc}}$ is the admittance of the dc-link capacitor. Steady-state values of the modulation index are defined in G_M. The power balance between the dc and ac sides is given in (32). Steady-state values can be determined according to (33). Notice that the DVC mainly influences d-axis elements in matrices, which can increase the imbalance between two eigenvalues

$$\begin{bmatrix} i_{\text{ref}}^{d,c} \\ i_{\text{ref}}^{q,c} \end{bmatrix} = \underbrace{\begin{bmatrix} F_{\text{DVC}} \\ 0 \end{bmatrix}}_{G_{\text{DVC}}} \left(v_{\text{dc,ref}} - v_{\text{dc}} \right) \tag{29}$$

$$\hat{v}_{\text{dc}} = \underbrace{\frac{3}{4} \begin{bmatrix} \frac{M^d}{Y_{\text{dc}}} & \frac{M^q}{Y_{\text{dc}}} \\ 0 & 0 \end{bmatrix}}_{G_{\text{DVC}}^{i}} \begin{bmatrix} \hat{i}_{L1}^{d} \\ \hat{i}_{L1}^{q} \end{bmatrix} + \underbrace{\frac{3}{4} \begin{bmatrix} \frac{I_{L1}^d}{Y_{\text{dc}}} & \frac{I_{L1}^q}{Y_{\text{dc}}} \\ 0 & 0 \end{bmatrix}}_{G_{\text{DVC}}^{m}} \begin{bmatrix} \hat{m}^{d,s} \\ \hat{m}^{q,s} \end{bmatrix} \tag{30}$$

$$G_M = \begin{bmatrix} M^d & M^q \end{bmatrix}^T \tag{31}$$

$$p = i_{\text{pv}} v_{\text{dc}} = \frac{3}{2} \left(i_{L1}^d m^d + i_{L1}^q m^q \right) \frac{v_{\text{dc}}}{2} \tag{32}$$

$$V_{\text{dc}} I_{\text{pv}} = \frac{3}{2} V_C^d I_{L1}^d. \tag{33}$$

1) Filter and Grid: The impedance and admittance of the LCL filter and grid are represented with following matrices:

$$Z_{L1} = \begin{bmatrix} sL_1 + R_1 & -\omega_g L_1 \\ \omega_g L_1 & sL_1 + R_1 \end{bmatrix} \tag{34}$$

$$Y_C = \begin{bmatrix} sC & -\omega_g C \\ \omega_g C & sC \end{bmatrix} \tag{35}$$

$$Z_{L2} = \begin{bmatrix} sL_2 + R_2 & -\omega_g L_2 \\ \omega_g L_2 & sL_2 + R_2 \end{bmatrix} \tag{36}$$

$$Z_g = \begin{bmatrix} sL_g + R_g & -\omega_g L_g \\ \omega_g L_g & sL_g + R_g \end{bmatrix}. \tag{37}$$

1) Inverter IM: Combining (18)–(28), the inverter impedance without the DVC is derived in (38), which applies to the analysis of the down-scale prototype. The IM considering the DVC is obtained by further including (29)–(33). Auxiliary functions given in (40)–(42) are used to facilitate expressions

$$Z_{\text{inv}} = \frac{G_{\text{del}}(G_{\text{ACC}} + G_{\text{dec}}) + Z_{L1}}{I - G_C} \tag{38}$$

$$Z_{\text{inv}} = \frac{(V_{\text{dc}}I - G_M G^m_{\text{DVC}})G_B - G_M G^i_{\text{DVC}} G_A - 2G_A Z_{L1}}{(V_{\text{dc}}I - G_M G^m_{\text{DVC}})G_C - 2G_A} \tag{39}$$

$$G_A = \frac{V_{\text{dc}}I}{2} - \frac{G_M G^m_{\text{DVC}}}{2} - G_{\text{del}} G_{\text{ACC}} G_{\text{DVC}} G^m_{\text{DVC}} \tag{40}$$

$$G_B = G_{\text{del}} G_{\text{ACC}} G_{\text{DVC}} G^i_{\text{DVC}} - G_{\text{del}} \left(G_{\text{ACC}} + G_{\text{dec}}\right) + \frac{G_M G^i_{\text{DVC}}}{2} \tag{41}$$

$$G_C = \frac{V_{\text{dc}} G^m_{\text{PLL}}}{2} + G_{\text{del}} G_{\text{VFF}} G^v_{\text{PLL}} - G_{\text{del}} G_{\text{AD}} \left(G^{ic}_{\text{PLL}} + Y_C\right) - G_{\text{del}} \left(G_{\text{ACC}} + G_{\text{dec}}\right) G^i_{\text{PLL}}. \tag{42}$$

REFERENCES

[1] H. Akagi, E. H. Watanabe, and M. Aredes, *Instantaneous Power Theory and Applications to Power Conditioning*. Hoboken, NJ, USA: Wiley, 2017.

[2] J. Holtz, "The representation of AC machine dynamics by complex signal flow graphs," *IEEE Trans. Ind. Electron.*, vol. 42, no. 3, pp. 263–271, Jun. 1995.

[3] F. B. Del Blanco, M. W. Degner, and R. D. Lorenz, "Dynamic analysis of current regulators for AC motors using complex vectors," *IEEE Trans. Ind. Appl.*, vol. 35, no. 6, pp. 1424–1432, Nov. 1999.

[4] F. Briz, M. W. Degner, and R. D. Lorenz, "Analysis and design of current regulators using complex vectors," *IEEE Trans. Ind. Appl.*, vol. 36, no. 3, pp. 817–825, May/Jun. 2000.

[5] J. Holtz *et al.*, "Design of fast and robust current regulators for high power drives based on complex state variables," in *Conf. Rec. 38th IAS Annu. Meeting Ind. Appl. Conf.*, 2003, vol. 3, pp. 1997–2004.

[6] S. Gataric and N. Garrigan, "Modeling and design of three-phase systems using complex transfer functions," in *Conf. Rec. 30th Annu. IEEE Power Electron. Specialists*, 1999, vol. 2, pp. 691–697.

[7] B. Wen, D. Boroyevich, R. Burgos, P. Mattavelli, and Z. Shen, "Analysis of dq small-signal impedance of grid-tied inverters," *IEEE Trans. Power Electron.*, vol. 31, no. 1, pp. 675–687, Jan. 2016.

[8] D. Lu, X. Wang, and F. Blaabjerg, "Impedance-based analysis of DC-link voltage dynamics in voltage-source converters," *IEEE Trans. Power Electron.*, vol. 34, no. 4, pp. 3973–3985, Apr. 2019.

[9] L. Harnefors, "Modeling of three-phase dynamic systems using complex transfer functions and transfer matrices," *IEEE Trans. Ind. Electron.*, vol. 54, no. 4, pp. 2239–2248, Aug. 2007.

[10] X. Wang, L. Harnefors, and F. Blaabjerg, "Unified impedance model of grid-connected voltage-source converters," *IEEE Trans. Power Electron.*, vol. 33, no. 2, pp. 1775–1787, Feb. 2018.

[11] L. Harnefors and H.-P. Nee, "Model-based current control of AC machines using the internal model control method," *IEEE Trans. Ind. Appl.*, vol. 34, no. 1, pp. 133–141, Jan./Feb. 1998.

[12] S. Shinnaka, "New "mirror-phase vector control" for sensorless drive of permanent-magnet synchronous motor with pole saliency," *IEEE Trans. Ind. Appl.*, vol. 40, no. 2, pp. 599–606, Mar./Apr. 2004.

[13] J. Lunze, *Regelungstechnik 1: Systemtheoretische Grundlagen, Analyse Und Entwurf Einschleifiger Regelungen*. Berlin, Germany: Springer, 2013.

[14] J. Shen, S. Schröder, H. Stagge, and R. W. De Doncker, "Precise modeling and analysis of dq-frame current controller for high power converters with low pulse ratio," in *Proc. IEEE Energy Convers. Congr. Expo.*, 2012, pp. 61–68.

[15] H. A. B. Siddique, M. J. R. Ahmad, and R. W. De Doncker, "Optimal control and filter sizing of a multi-megawatt medium-voltage voltage-source converter for future grids," in *Proc. IEEE 7th Int. Symp. Power Electron. Distrib. Gener. Syst.*, 2016, pp. 1–8.

[16] P. Schülting, C. H. van der Broeck, and R. W. De Doncker, "Analysis and design of repetitive controllers for applications in distorted distribution grids," *IEEE Trans. Power Electron.*, vol. 34, no. 1, pp. 996–1004, Jan. 2018.

[17] C. Zhang, X. Cai, A. Rygg, and M. Molinas, "Sequence domain SISO equivalent models of a grid-tied voltage source converter system for small-signal stability analysis," *IEEE Trans. Energy Convers.*, vol. 33, no. 2, pp. 741–749, Jun. 2018.

[18] H. Zhang, L. Harnefors, X. Wang, H. Gong, and J.-P. Hasler, "Stability analysis of grid-connected voltage-source converters using SISO modeling," *IEEE Trans. Power Electron.*, vol. 34, no. 8, pp. 8104–8117, Aug. 2019.

[19] L. Huang *et al.*, "Grid-synchronization stability analysis and loop shaping for PLL-based power converters with different reactive power control," *IEEE Trans. Smart Grid*, vol. 11, no. 1, pp. 501–516, Jan. 2020.

[20] D. Yang, X. Wang, F. Liu, K. Xin, Y. Liu, and F. Blaabjerg, "Symmetrical PLL for SISO impedance modeling and enhanced stability in weak grids," *IEEE Trans. Power Electron.*, vol. 35, no. 2, pp. 1473–1483, Feb. 2020.

[21] J. Lunze, *Regelungstechnik 2: Mehrgrößensysteme, Digitale Regelung*. Berlin, Germany: Springe-Verlag, 2010.

[22] Z. Yang, C. Shah, T. Chen, L. Yu, P. Joebges, and R. W. De Doncker, "Stability investigation of three-phase grid-tied PV inverter systems using impedance models," *IEEE J. Emerg. Sel. Topics Power Electron.*, to be published, doi: 10.1109/JESTPE.2020.3047964.

[23] J. Sun, "Impedance-based stability criterion for grid-connected inverters," *IEEE Trans. Power Electron.*, vol. 26, no. 11, pp. 3075–3078, Nov. 2011.

[24] J. R. Bar-on and E. Jonckheere, "Gain margins for multivariable control systems," in *Proc. 29th IEEE Conf. Decis. Control*, 1990, pp. 340–347.

[25] J. R. Bar-on and E. A. Jonckheere, "Phase margins for multivariable control systems," *Int. J. Control*, vol. 52, no. 2, pp. 485–498, 1990.

[26] Z. Liu, J. Liu, W. Bao, and Y. Zhao, "Infinity-norm of impedance-based stability criterion for three-phase AC distributed power systems with constant power loads," *IEEE Trans. Power Electron.*, vol. 30, no. 6, pp. 3030–3043, Jun. 2015.

[27] Y. Zhou, H. Hu, J. Yang, and Z. He, "A novel forbidden-region-based stability criterion in modified sequence-domain for AC grid-converter system," *IEEE Trans. Power Electron.*, vol. 34, no. 4, pp. 2988–2995, Apr. 2019.

[28] A. G. MacFarlane and I. Postlethwaite, "The generalized Nyquist stability criterion and multivariable root loci," *Int. J. Control*, vol. 25, no. 1, pp. 81–127, 1977.

[29] M. Belkhayat, "Stability criteria for AC power systems with regulated loads," Ph.D. dissertation, Purdue University, West Lafayette, NI, USA, 1997.

[30] *IEEE Recommended Practice for Utility Interface of Photovoltaic (PV) Systems*, IEEE Std 929-2000, 2000.

Zhiqing Yang (Student Member, IEEE) received the B.S. degree from Southwest Jiaotong University, Chengdu, China, in 2013 and the M.S. degree from RWTH Aachen University, Aachen, Germany, in 2017, both in electrical engineering.

From April to September 2016, he was an Intern with the Advanced Technology R&D Center, Mitsubishi Electric, Amagasaki, Japan. In 2017, he joined with the Institute for Power Generation and Storage Systems, E.ON Energy Research Center, RWTH Aachen University, as a Research Associate. His research interests include modeling and control of power electronic system for renewable energy applications.

Tianxiao Chen (Student Member, IEEE) received the B.S. degree from Zhejiang University, Hangzhou, China, in 2017, and the M.S. degree from RWTH Aachen University, Aachen, Germany, in 2020, both in electrical engineering.

His research interests include stability analysis and improvement, renewable energy applications.

Xian Luo received the B.S. degree from Tsinghua University, Beijing, China, in 2016, and the M.S. degree from the Institute for Power Generation and Storage Systems, E.ON Energy Research Center, RWTH Aachen University, Aachen, Germany, in 2020, both in electrical engineering.

From September 2019 to March 2020, she was an Intern with the Advanced Technology Laboratory, Corporate R&D Headquarters, Fuji Electric Co., Ltd, Tokyo, Japan. Her research interests include modeling and control of power electronic system for renewable energy applications.

Philipp Schülting received the B.Sc., M.Sc., and Ph.D. degrees from RWTH Aachen University, Aachen, Germany, in 2014 and 2020, all in electrical engineering.

From January 2015 to September 2020, he was with the Institute for Power Electronics and Electrical Drives, RWTH Aachen University. His research interests include the field of power electronics and control.

Rik W. De Doncker (Fellow, IEEE) received the Ph.D. degree in electrical engineering from Katholieke Universiteit Leuven, Leuven, Belgium, in 1986.

In 1987, he was a Visiting Associate Professor with the University of Wisconsin, Madison, Madison, WI, USA. He was an Adjunct Researcher with the Interuniversity Microelectronics Centre, Leuven, Belgium. In 1989, he was with the Corporate Research and Development Center, General Electric Company, Schenectady, NY, USA. In 1994, he was the Vice President of Technology with the Silicon Power Corporation, a former division of General Electric Inc. In 1996, he was a Professor with RWTH Aachen University, Aachen, Germany, where he currently leads the Institute for Power Electronics and Electrical Drives. Since 2006, he has been the Director with the E.ON Energy Research Center, RWTH Aachen University. In 2009, he led a VDE/ETG Task Force on electric vehicles.

Dr. De Doncker was the President of the IEEE Power Electronics Society (PELS) in 2005 and 2006. He was the Founding Chairman of the German IEEE Industry Applications Society PELS Joint Chapter. In 2002, he was the recipient of the IEEE IAS Outstanding Achievement Award, the IEEE PES Nari Hingorani Custom Power Award, in 2008, the IEEE William E. Newell Power Electronics Award, in 2013, and the IEEE Medal in Power Engineering, in 2020.